Electronic Supplementary Material (ESI) for ChemComm.
This journal is © The Royal Society of Chemistry 2015

Electronic Supplementary Information for

Photocatalytic Hydrogen Evolution over β-Iron Silicide under Infrared-Light Irradiation

Masaharu Yoshimizu,[a] Ryoya Kobayashi,[a] Makoto Saegusa,[a] Toshihiro Takashima,[b] Hiroshi Funakubo,[c] Kensuke Akiyama,[d] Yoshihisa Matsumoto[d] and Hiroshi Irie*[b,e]

[a] Interdisciplinary Graduate School of Medicine and Engineering, University of Yamanashi, 4-3-11 Takeda, Kofu, Yamanashi 400-8511, Japan

[b] Department of Innovative and Engineering Materials, Tokyo Institute of Technology, 4259 Nagatsuda, Midori-ku, Yokohama, Kanagawa 266-8502, Japan

[c] Kanagawa Industrial Technology Center, 705-1 Shimoizumi, Ebina, Kanagawa 243-0435, Japan

[d] Clean Energy Research Center, University of Yamanashi, 4-3-11 Takeda, Kofu, Yamanashi 400-8511, Japan

[e] Japan Science and Technology Agency (JST), Core Research for Evolutionary Science and Technology (CREST), 5 Sanbancho, Chiyoda-ku, Tokyo 102-0075, Japan

Contents

ESI-1) SEM images of as-purchased and pulverized β-$FeSi_2$ powders (Figs. S1a and S1b).
ESI-2) UV-visible absorption spectrum of pulverized β-$FeSi_2$ powder (Figs. S2a and S2b).
ESI-3) Preparation of β-$FeSi_2$ thin films and electrical conducting type of β-$FeSi_2$ thin film and powder.
ESI-4) pH dependence of the stability of β-$FeSi_2$ powder in dark conditions (Fig. S3).
ESI-5) Detailed procedures and additional comments for photocatalytic water-splitting tests (Figs. S4 and S5, Tables S1 and S2).
ESI-6) Detailed procedures of testing and evaluating stability in the dark and under light irradiation using XPS (Figs. S6-S10, Table S3).
ESI-7) TEM observations of β-$FeSi_2$ powders before and after photocatalytic reaction (Fig. S11).

ESI-1) SEM images of as-purchased and pulverized β-$FeSi_2$ powders (Figs. S1a and S1b).

A scanning electron microscope (SEM, S-4500; Hitachi) was used to observe the as-purchased and pulverized β-$FeSi_2$ powders. The crystallite sizes of the as-purchased powder ranged from several to several tens of micrometers (Fig. S1a). After pulverization, the crystallite sizes decreased to several micrometers (Fig. S1b).

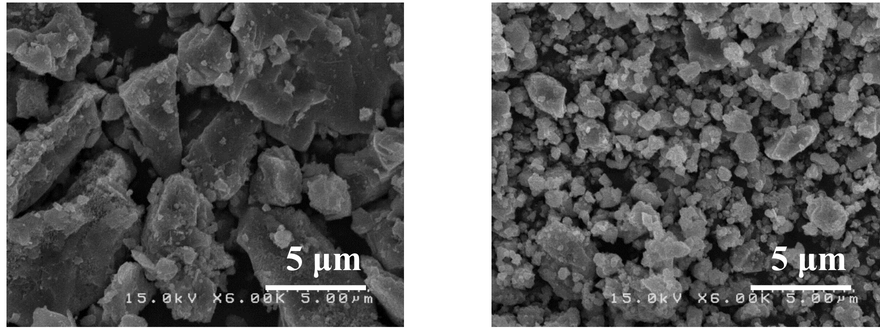

Figure S1. SEM images of the as-purchased (a, left) and pulverized β-$FeSi_2$ powders (b, right).

ESI-2) UV-visible absorption spectrum of pulverized β-$FeSi_2$ powder (Figs. S2a and S2b).

A UV-visible absorption spectrum (UV-vis) of pulverized β-$FeSi_2$ powder was obtained by the diffuse reflection method using a spectrometer (V-670; JASCO) and $BaSO_4$ as a reflectance standard (Fig. S2a and inset). To extract the direct band-gap energy, $(h\nu\alpha)^2$ is typically plotted as a function of photon energy ($h\nu$). According to the literature, β-$FeSi_2$ is a direct semiconductor. In the $(h\nu\alpha)^2$ vs. $h\nu$ plot shown in Fig. S2b, the tangent line extrapolated to $(h\nu\alpha)^2 = 0$ indicates the band gap, in this case ~ 0.80 eV, which corresponds the reported value. As the band-gap of β-$FeSi_2$ is 0.80 eV, it is reasonable that β-$FeSi_2$ can absorb the wavelength range up to 1550 nm.

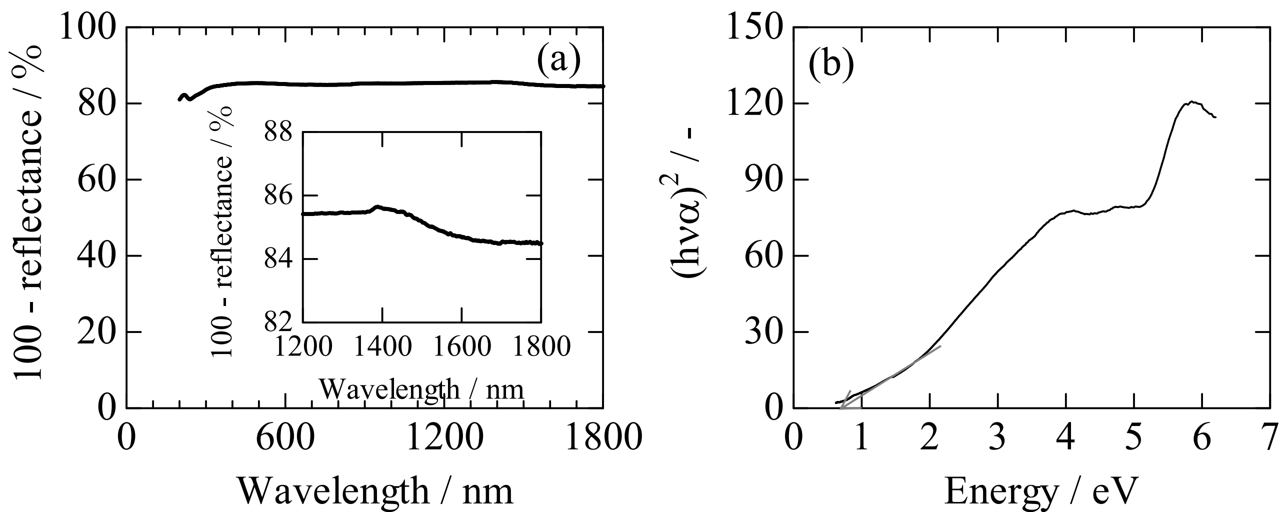

Figure S2. UV-vis absorption spectrum of pulverized β-$FeSi_2$ powder (a). An enlargement of the spectrum is shown in the inset. $(h\nu\alpha)^2$ plot for (a) calculated by the Kubelka-Munk conversion of reflectance (b).

ESI-3) Preparation of β-$FeSi_2$ thin films and electrical conducting type of β-$FeSi_2$ thin film and powder.

The preparation procedure for the β-$FeSi_2$ thin film and characterizations of the as-deposited film were previously reported by two of the present authors (K. A. and H. F.).[10] Briefly, a silver (Ag) layer was deposited on silicon (100) (Si(100)) substrate at room temperature under vacuum atmosphere (< 6.7×10^{-4} Pa). β-$FeSi_2$ thin films with a thickness of ~ 150 nm were deposited on the Ag-coated Si(100) substrate at a temperature of 760°C using a metal organic chemical vapor deposition (MOCVD) method with iron pentacarbonyl [$Fe(CO)_5$] and mono-silane (SiH_4) as sources of Fe and Si, respectively, under H_2 flow. The deposited β-$FeSi_2$ thin films were annealed at 760°C for 4 h under vacuum conditions (<6.7×10^{-4} Pa). XRD, photoluminescence spectroscopty and transmission electron microscopy (TEM) characterizations

of the as-prepared β-$FeSi_2$ thin films were performed as previously described.[10] In addition, K. A. and H. F. reported the p-type semiconducting property of β-$FeSi_2$ thin film by measuring the Hall coefficient using a method of van der Pauw.[i]

As for the pulverized β-$FeSi_2$ powder, we evaluated its semiconducting property by measuring the Seebeck coefficient (*S*) using a conventional two-probe steady-state method. The pulverized powder was uniaxially pressed into a rectangular pellet with the dimensions ~ 4 × 5 × 20 mm, followed by calcination at 800 °C for 2 h under vacuum conditions ($<1.1\times10^{-3}$ Pa). To measure *S*, two Pt wires were attached by an Ag-conductive region to the prepared rectangular pellet. At 50 °C, we confirmed the positive sign of *S*, indicating the p-type semiconductor, and the *S* value of ~ 4 μV K^{-1}.

ref. i) K. Akiyama, S. Kaneko, T. Ozawa, H. Funakubo and Y. HIrabayashi, Abstract Book of the 72th the Japan Society of Applied Physics (JSAP) Autumn Meeting, 2011, 1p-W-5.

ESI-4) pH dependence of the stability of β-$FeSi_2$ powder in dark conditions (Fig. S3).

The pH dependence of β-$FeSi_2$ for H_2 evolution was conducted in a gas-closed circulation system in the dark. β-$FeSi_2$ powder (60 mg) was suspended in 12 mL aqueous solution (pH 1, 3, 4, 7, and 10; adjusted using H_2SO_4 and NaOH) using a magnetic stirrer. Argon gas (50 kPa) was introduced into the system after deaeration to a final pressure of 2.5 Pa. The amounts of evolved H_2 were monitored using an online gas chromatograph (GC-8A; Shimadzu).

At pH 1, the unexpected H_2 evolution was observed. The clear reason is not known yet, however the plausible reason would be as follows by the analogy with the previous literature[ii]; in the literature, H_2 was produced by boiling Fe-20%Si alloy in the high-concentrated H_2SO_4 (50% H_2SO_4), forming the passive film on its surface composed of O and Si-oxide. In the present study, it would be probable to consider that the similar reaction proceeds in the H_2SO_4 solution at pH 1.

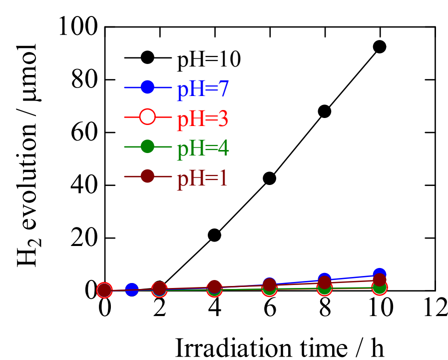

Figure S3. Time courses of H_2 evolution at pH 1, 3, 4, 7, and 10.

ref. ii) I. Ioka, J. Mori, C. Kato, M. Futakawa, K. Onuki, *J. Mater. Sci. Lett.*, 1999, **18**, 1497.

ESI-5) Detailed procedures and additional comments for photocatalytic water-splitting tests (Figs. S4 and S5, Tables S1 and S2).

Photocatalytic overall water-splitting tests were conducted in a gas-closed circulation system. Photocatalyst powder (60 mg) was suspended in 12 mL acidic aqueous solution (pH 3; adjusted using H_2SO_4) containing a sacrificial agent (0.1 M HCHO or 0.3 M $S_2O_6^{2-}$ ($Na_2S_2O_6$)) using a magnetic stirrer. Argon gas (50 kPa) was introduced into the system after repeated deaeration to a final pressure of 2.5 Pa. A xenon lamp (LA-251Xe; Hayashi Tokei) equipped with an optical filter (O-58) was employed for light irradiation at wavelengths longer than 560 nm and a halogen-tungsten lamp (ASBN Series; Spectral Products) equipped with a long-pass filter (BLP01-1319R-25, Semrock Inc.) was used for light irradiation at wavelengths longer than 1300 nm.

Additionally, H_2 evolution reactions in the presence of $S_2O_6^{2-}$ (0.3 M) were measured under monochromatic light to examine the wavelength dependence of the quantum efficiency (QE) using a Czerny-Turner type monochromator (MC-10N; Ritsu Ouyou Kogaku) and the xenon or halogen-tungsten lamp. Monochromatic light with wavelengths of 440±10, 520±10, 600±10, 680±10 (xenon lamp), and 950±25 nm (halogen-tungsten lamp), and an intensity of ~ 100 μW/cm^2 was used for the reactions. The light intensity was corrected using a spectroradiometer (USR-40, Ushio). Higher order diffracted light was cutoff with the appropriate glass filter. The amount of evolved H_2 was monitored using the GC-8A online gas chromatograph. The apparent quantum efficiency (AQE) value for H_2 evolution was calculated using the equation AQE (%) = 2 × H_2 evolution rate / absorption rate of incident photon × 100, because H_2 evolution is represented by the formula $2H^+ + 2e^- \rightarrow H_2$.

When using $S_2O_6^{2-}$ as the sacrificial agent, H_2 evolution was initially supressed, but then gradually increased (Figs. 1a and 1b). In contrast, when HCHO was used as the sacrificial agent, the induction period for H_2 evolution was not observed. Although the reason for the delay in H_2 evolution was unclear, it may have been due to reduced photocatalytic activity of β-$FeSi_2$ by the poisonous effect of S species. When the photocatalyst was soaked in $S_2O_6^{2-}$ solution, the active

site for H_2 evolution was occupied by the sulfur species. However, during irradiation, such S species were removed by the oxdative decomposition and/or were scarcely adsorbed on the photocatalyst surface, which was partially oxidized and stabilized, as discussed in the main text in relation to the results presented in Fig. 3. Supporting this speculation, in the second cycle shown in Fig. 1a, the induction period was not observed.

The redox potentials of $S_2O_6^{2-}$ and HCHO are –0.253 V (vs. SHE, $E^0(S_2O_6^{2-}/SO_4^{2-}) = -0.253$, $S_2O_6^{2-} + 2H^+ + 2e^- \rightarrow 2SO_4^{2-}$, pH = 0) and 0.056 V (vs. SHE, E^0(HCOOH/HCHO) = 0.056, $HCOOH + 2H^+ + 2e^- \rightarrow HCHO$, pH = 0), respectively.[a] Thus, the photo-generated holes in the VB of β-$FeSi_2$ (VB top potential ~ 0.15 V vs. SHE) can oxidize $S_2O_6^{2-}$ and HCHO. The redox potential of the sacrificial agent would affect the H_2 evolution activity, as $S_2O_6^{2-}$ is more easily oxidized than HCHO, resulting in a higher H_2 evolution rate.

Figure S4 shows the amount of H_2 evolved by β-$FeSi_2$ under monochromatic light with wavelengths of 440±10, 520±10, 600±10, 680±10, and 950±25 nm, and an intensity of ~ 100 μW/cm^2 at pH 3 in the presence of $S_2O_6^{2-}$ (0.3 M), and 600±10 and 950±25 nm at pH 3 in the presence of HCHO (0.1 M). The reaction under 600±10-nm light in the presence of $S_2O_6^{2-}$ was repeated twice to confirm the reproducibility of the photocatyltic reaction. We calculated the number of photons that β-$FeSi_2$ could absorb on irradiation with the monochromatic light (440±10, 520±10, 600±10, 680±10, and 950±25 nm, Tables S1, S2). We calculated the H_2 evolution rates from the slopes of the straight lines in Fig. S4 and then estimated the AQE values using the above mentioned equation (Tables S1, S2). The AQE values were ~ 25-30 % and ~ 10 % in the presence of $S_2O_6^{2-}$ and HCHO, respectively. The order of these AQE values was proved to be identical. Note that the values did not change so much regardless of the wavelengths of monochromatic lights. In addition, the results coincided with the previous discussion that the redox potential of the sacrificial agent would affect the H_2 evolution activity, as $S_2O_6^{2-}$ is more easily oxidized than HCHO, resulting in a higher H_2 evolution rate.

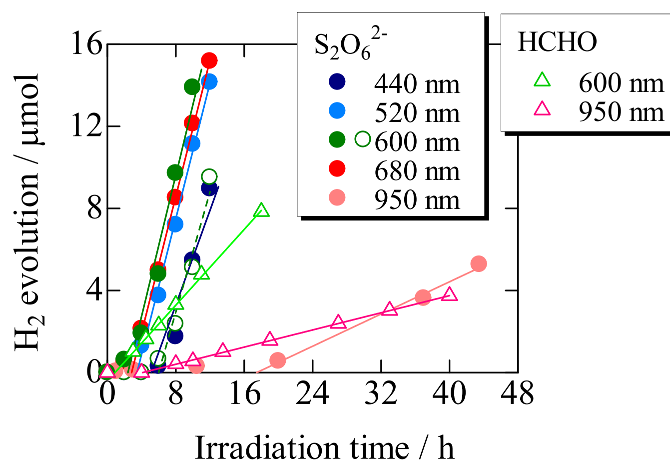

Figure S4. Time courses of H_2 evolution under monochromic lights with wavelengths of 440±10, 520±10, 600±10, 680±10, and 950±25 nm.

Table S1. H_2 generation rates in the presence of $S_2O_6^{2-}$ under 440±10, 520±10, 600±10, 680±10, and 950±25 nm monochromic lights, absorbed photon numbers and AQE values.

Irradiated light / nm	H_2 generation rate / μmol h^{-1}	Absorbed photon number / quanta s^{-1}	AQE / %
440±10	1.15	1.44×10^{15}	26.7
520±10	1.65	1.79×10^{15}	30.9
600±10	1.72	2.06×10^{15}	27.8
	1.37	2.06×10^{15}	22.1
680±10	1.66	2.31×10^{15}	24.0
950±25	1.96×10^{-1}	2.68×10^{14}	24.5

Table S2. H_2 generation rates in the presence of HCHO under 600±10 and 950±25 nm monochromic lights, absorbed photon numbers and AQE values.

Irradiated light / nm	H_2 generation rate / μmol h^{-1}	Absorbed photon number / quanta s^{-1}	AQE / %
600±10	4.62×10^{-1}	1.86×10^{15}	8.31
950±25	9.94×10^{-2}	2.42×10^{14}	13.7

The photocatalytic water-splitting test was also conducted using deuterium oxide (D_2O, 99.9 atom% D) in a gas-closed circulation system. Photocatalyst powder (60 mg) was suspended in 12 mL acidic D_2O solution (pH 3; adjusted using H_2SO_4) containing 0.3 M $S_2O_6^{2-}$ under visible light irradiation (> 560 nm, Xe-lamp + O-58). After 120 h irradiation, the evolved D_2 was detected by a mass spectrometer (MS, Prisma Plus QMG220, Pfeiffer). Figure S5 shows the result, accompanied by a controlled experiment without light irradiation. The evolution of D_2 was clearly detected, indicating that the detected H_2 was originated from H_2O in Figs. 1 and 2. Note that the detected Ar was originated from the carrier gas. Although N_2 and O_2 were unexpectedly detected, the N_2 and O_2 in the system likely originated from external air that entered the MS system at the so-called "splitter" component, which is the site of sample injection, or from internal air remaining in the system.

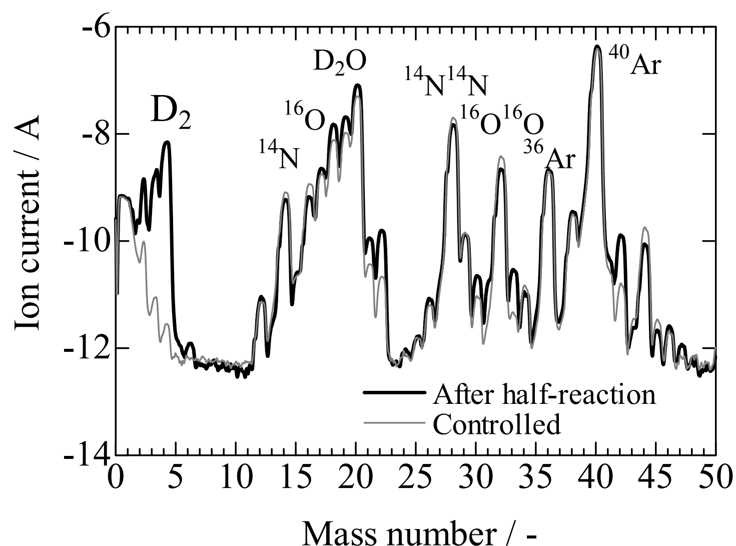

Figure S5. The GCMS profile using D_2O as a result of the half-reaction of water, accompanied by the controlled experiment without the reaction.

ref. a) A. J. Bard, R. Parsons and J. Jordan, *Standard Potentials in Aqueous Solution*, 1985, New York: Marcel Dekker.

ESI-6) Detailed procedures of testing stability in the dark and under light irradiation using XPS (Figs. S6-S10, Table S3).

The Si $2p_{3/2}$, Si$2p_{1/2}$, Fe $2p_{3/2}$, and O 1s core levels were measured by X-ray photoelectron spectroscopy (XPS; JEOL, JPS-9200) on the surface of the as-deposited β-$FeSi_2$ thin film to examine the percentages of Si^0, Si^{2+}, Si^{3+}, Si^{4+}, Fe^0, Fe^{2+}, and O (Fig. S6). The film was then immersed in 12 mL acidic aqueous solution (pH 3, adjusted using H_2SO_4) containing a sacrificial agent (0.1 M HCHO) for 24 h in the dark, and XPS measurements of the same core levels were again performed (Fig. S6). After the measurments, the film was immersed in the acidic solution containin 0.1 M HCHO, and was then irradiated with light from a xenon light for 36 h without optical filters. HCHO was selected as a sacrificial agent to avoid detecting S species by XPS. To accelerate the water-splitting reaction, we utilized unfiltered light from the xenon light. At intervals during the irradiation, the surface was subjected to XPS measurements (Fig. S6). After 36-h irradiation, the surface and inner region up to ~ 7.8 nm from the surface involving "in-situ Ar^+ etching" were measured by XPS (Fig. S7). The etching rate was 1.2 nm/min. For comparison, the surface of the newly prepared as-deposited thin film and inner areas up to ~ 7.8 nm from the surface with in-situ Ar^+etching were also measured by XPS (Fig. S8). All spectral binding energies were referenced to the Si 2p peak (Si$2p_{3/2}$+Si$2p_{1/2}$), which had a binding energy of 99.9 eV.

The reported Si $2p_{3/2}$ and Si$2p_{1/2}$ binding energies of Si^0 (silicon) are 99.6 and 100.2 eV, respectively.[A-C] As for Si sub-oxides (SiO, Si_2O_3 and SiO_2), the Si 2p binding energies in SiO (Si^{2+}), Si_2O_3 (Si^{3+}) and SiO_2 (Si^{4+}) are 101.4-102.0, 102.1-102.7 and 103.5-104.1 eV, respectively.[A-C] In the present study, the Si 2p peak arising from Si^0 was fit with two peaks (Si $2p_{3/2}$ and Si$2p_{1/2}$), and the oxidized Si peaks were fit with a single peak (Si 2p) after ref. D. To quantitatively evaluate the Si^0, Si^{2+}, Si^{3+} and Si^{4+} atomic percentages, peak deconvolution was performed using a Gaussian lineshape with the following parameters. The binding energies of Si $2p_{3/2}$ and Si$2p_{1/2}$ of Si^0 in β-$FeSi_2$, Si 2p of SiO (Si^{2+}), Si_2O_3 (Si^{3+}) and SiO_2 (Si^{4+}) were fixed at 99.7±0.1, 100.3±0.1, 101.8±0.1, 102.8±0.1 and 104.0±0.1 eV (the binding energy of Si 2p in β-$FeSi_2$ is slightly larger than that of Si 2p in Si, SiO, Si_2O_3 and SiO_2),[E] and the peak area ratio of Si $2p_{1/2}$ to Si $2p_{3/2}$ was fixed at 0.50±0.01.[D] The Si^0, Si^{2+}, Si^{3+} and Si^{4+} areas were determined from those of each Si$2p_{3/2}$ peak. As the oxidized Si peaks (Si^{2+}, Si^{3+} and Si^{4+}) were fit with the single peak (Si 2p), the area of each Si $2p_{3/2}$ was calculated to be two-thirds of each area of Si 2p (Si^{2+}, Si^{3+} and Si^{4+}).

Fe $2p_{3/2}$ binding energies in β-$FeSi_2$ (Fe^0) and FeO (Fe^{2+}) are 707.3-707.5 and 709.2 eV, respectively.[E-G] Thus, the peak deconvolution was similarly performed using a Gaussian lineshape by fixing the binding energies at 707.3±0.1 and 709.0±0.1 eV for Fe^0 and Fe^{2+}, respectively. The Fe^0 and Fe^{2+} ratio was then determined from the area of each Fe2p3/2 peak. The O 1s peak was not adopted in the peak fit method, and we simply utilized the peak area.

Si^0, Si^{2+}, Si^{4+}, Fe^0, Fe^{2+}, and O percentages were determined by considering each peak area and the sensitivity factors of Si$2p_{3/2}$ (3.3997), Fe $2p_{3/2}$ (38.987), and O1s (11.2659).

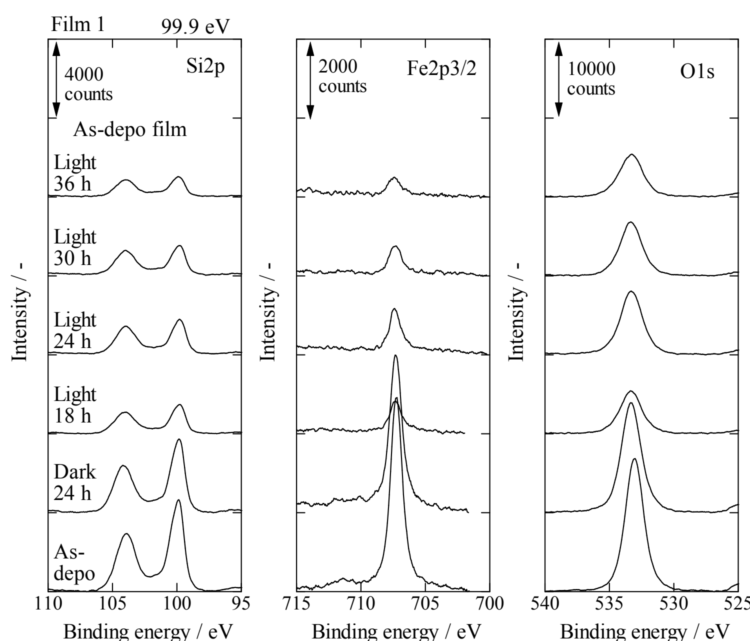

Figure S6. Si 2p (left), Fe 2p3/2 (middle), and O 1s (right) XPS spectra of as-deposited β-$FeSi_2$, β-$FeSi_2$ after dark storage in pH 3 aqueous solution with a sacrificial agent (0.3 M $S_2O_6^{2-}$) for 24 h, and after xenon light irradiation for 18, 24, 30 and 36 h in the same solution, respectively.

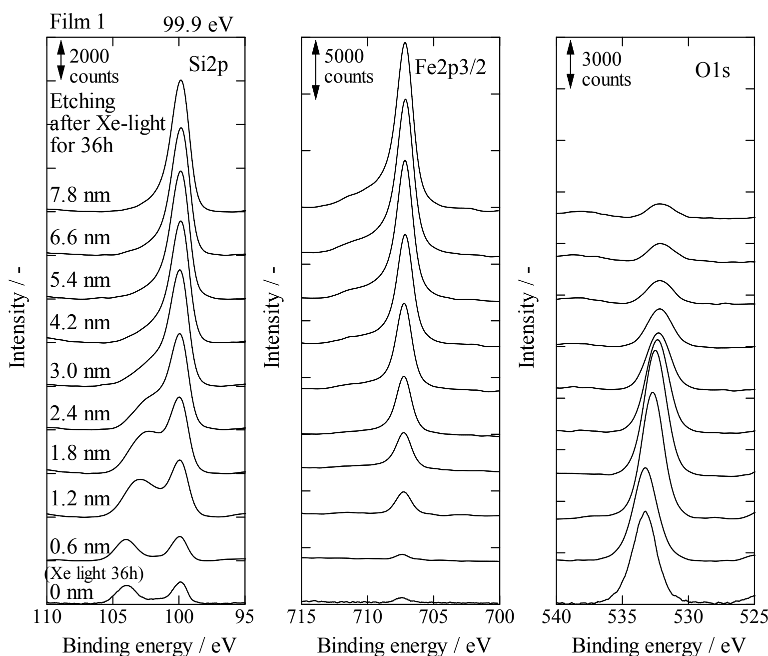

Figure S7. Si 2p (left), Fe 2p3/2 (middle), and O 1s (right) XPS spectra of β-$FeSi_2$ after xenon light irradiation for 36 h in pH 3 aqueous solution with a sacrificial agent (0.3 M $S_2O_6^{2-}$) and after etching 0.6-7.8 nm from the surface.

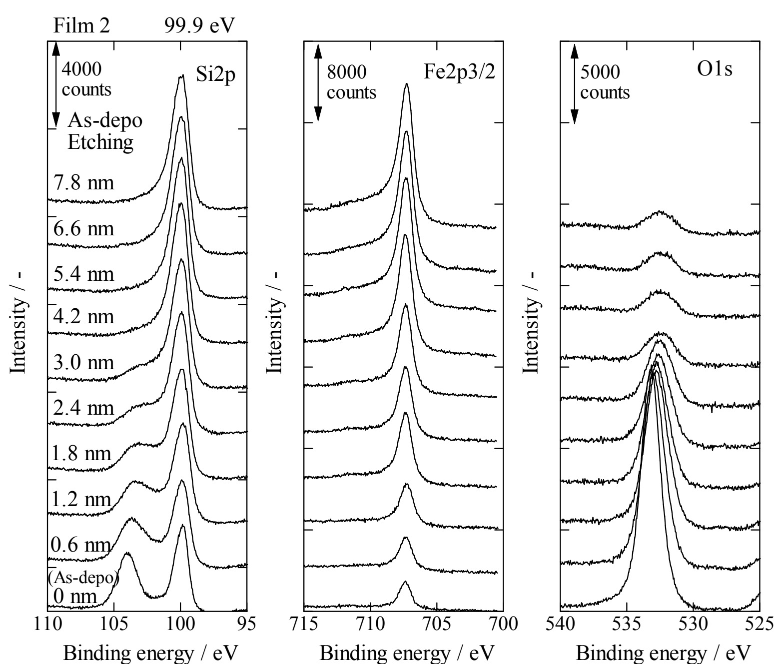

Figure S8. Si 2p (left), Fe 2p3/2 (middle), and O 1s (right) XPS spectra of the surface of as-deposited β-$FeSi_2$ (etching, 0 nm) and after etching 0.6-7.8 nm from the surface.

References

[A] O. M. Nemtsova and O. M. Kanunnikova, *J. Struc. Chem.*, 2011, **52**, Suppl., S16.
[B] F. J. Himepsel, F. R. McFeely, A. Taleb-Ibrahimi and J. A. Yamoff, *Phys. Rev. B*, 1988, **38**, 6084.
[C] F. Esaka, H. Yamamoto, N. Matsibayashi, Y. Yamada, M. Sasae, K. Yamaguchi, S. Shamoto, M. Magara and T. Kimura, *Appl. Surf. Sci.*, 2010, **256**, 3155.
[D] J. A. Haber and N. S. Lewis, *J. Phys. Chem. B*, 2002, **106**, 3639.
[E] V. Kinsinger, I. Dezsi, P. Steiner and G. Langouche, *J. Phys.: Condens. Matter.*, 1990, **2**, 4955.
[F] A. Toneva, E. Goranova, G. Beshkov, T. Marinova and A. Kakanakova-Georgieva, *Vacuum*, 2000, **58**, 420.
[G] N. Ohtsu, M. Oku, K. Satoh and K. Wagatsuma, *Appl. Surf. Sci.*, 2013, **264**, 219.
[H] H. Yu, H. Irie, Y. Shimodaira, Y. Hosogi, Y. Kuroda, M. Miyauchi, K. Hashimoto, *J. Phys. Chem. C*, 2010, **114**, 16481.

The peak deconvolution results are shown in Table S3, and Figs. S9 and S10. The abbreviated designation of each peak deconvolution is indicated in the left column in Table S1 above the graphs in Fig. S9. In Table S3, the peak positions (eV), areas, and full widths at half maximum (FWHM, eV) for each contribution to the deconvolution are shown. The peak area ratios of Si $2p_{1/2}$ to Si $2p_{3/2}$ derived from Si^0 are also indicated.
The plotted experimental data (open gray circles), fitted curves (i.e., the calculated sum of the contributions of the deconvolution, bold black lines), and component peaks (thin solid lines) determined by deconvolution of the experimental data are shown. Thus, the calculated sum of each thin black line equals that of the corresponding bold black solid line. The plotted experimental data (open gray circles) and fitted curves (bold black lines) coincided well. For Fe $2p_{3/2}$, when FeO was not included in the deconvolution, only the fitted curves were drawn.

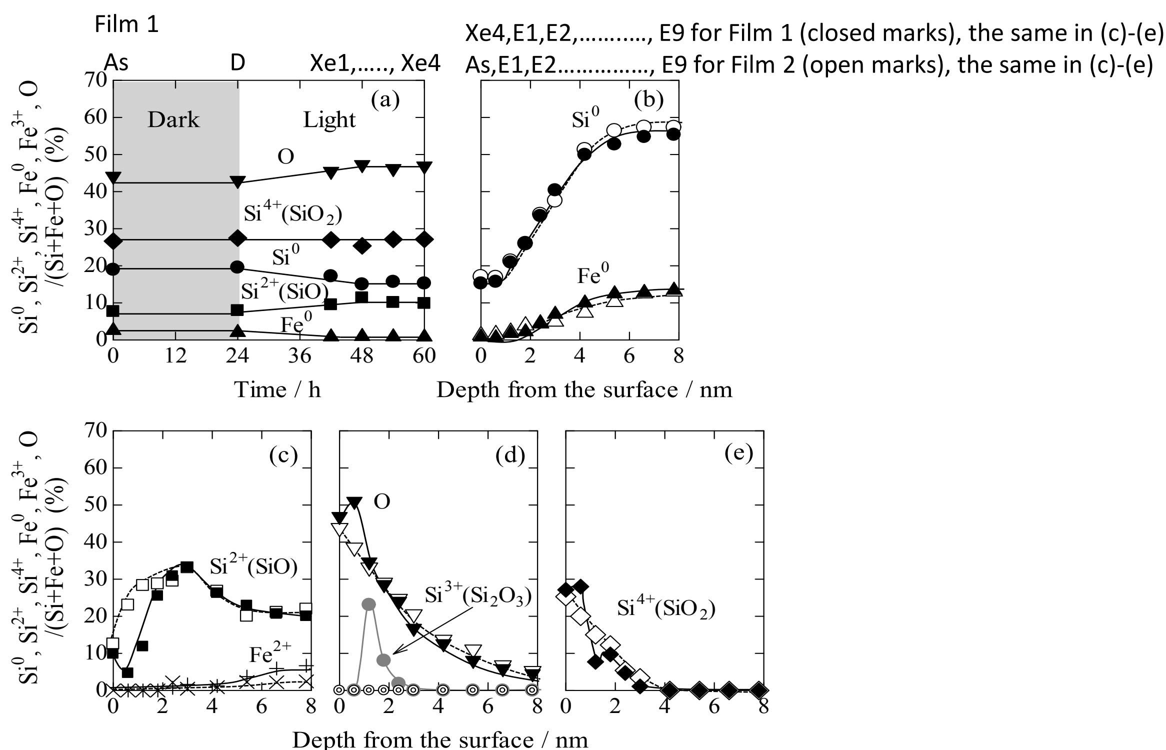

Figure S7. The abbreviated designations of each plot are indicated above the graphs. These graphs are identical to those presented in Figs. 3 in the main text.

Table S3. Peak positions (eV), areas, and full widths at half maximum (FWHM, eV) for each contribution to the deconvolution, and the peak area ratios of Si $2p_{1/2}$ to Si $2p_{3/2}$ derived from Si^0.

			Si	Si	SiO	Si_2O_3	SiO_2	$FeSi_2$	FeO
			$Si2p_{3/2}$	$Si2p_{1/2}$	$Si2p_{3/2}+Si2p_{1/2}$	$Si2p_{3/2}+Si2p_{1/2}$	$Si2p_{3/2}+Si2p_{1/2}$	$Fe2p_{3/2}$	$Fe2p_{3/2}$
Film 1 As	As-depo	Position/eV	99.8	100.4	101.7	=	103.9	707.3	=
		Area	3150	1570	1280	=	4420	4920	=
		Width (FWHM)/eV	0.83	0.83	3.00	=	1.67	1.07	=
			(Si2p1/2)/(Si2p3/2)= 0.50						
D	Dark 24h	Position/eV	99.8	100.4	101.8	=	104.1	707.3	=
		Area	2930	1460	1570	=	3920	3740	=
		Width (FWHM)/eV	0.92	0.92	3.00	=	1.68	1.06	=
			(Si2p1/2)/(Si2p3/2)= 0.50						
Xe1	Xe 18h	Position/eV	99.8	100.4	101.9	=	104.1	707.4	=
		Area	1239	608	685	=	1943	698	=
		Width (FWHM)/eV	1.01	1.14	3.00	=	1.81	1.01	=
			(Si2p1/2)/(Si2p3/2)= 0.49						
Xe2	Xe 24h	Position/eV	99.7	100.4	101.8	=	104.1	707.4	=
		Area	1330	665	1010	=	2250	965	=
		Width (FWHM)/eV	0.97	0.93	3.00	=	1.74	1.00	=
			(Si2p1/2)/(Si2p3/2)= 0.50						
Xe3	Xe 30h	Position/eV	99.8	100.4	101.9	=	104.1	707.4	=
		Area	1210	617	780	=	2090	761	=
		Width (FWHM)/eV	0.98	1.00	2.83	=	1.76	1.10	=
			(Si2p1/2)/(Si2p3/2)= 0.51						
Xe4	Xe 36h	Position/eV	99.8	100.4	101.8	=	104.0	707.4	=
	(Etching 0 nm)	Area	794	398	513	−	1410	487	=
		Width (FWHM)/eV	0.92	0.89	2.50	−	1.66	1.17	=
			(Si2p1/2)/(Si2p3/2)= 0.50						
E1	Etching 0.6 nm	Position/eV	99.8	100.3	101.7	=	104.0	707.4	=
		Area	1080	545	320	=	1920	487	=
		Width (FWHM)/eV	1.24	1.25	1.67	=	1.87	1.11	=
			(Si2p1/2)/(Si2p3/2)= 0.50						
E2	Etching 1.2 nm	Position/eV	99.8	100.4	101.6	102.8	103.4	707.3	=
		Area	2710	1360	1540	2990	1000	2660	=
		Width (FWHM)/eV	1.42	1.42	2.41	2.31	1.77	1.36	=
			(Si2p1/2)/(Si2p3/2)= 0.50						
E3	Etching 1.8 nm	Position/eV	99.7	100.3	101.9	102.9	103.9	707.3	=
		Area	4150	2070	4070	1280	1550	4110	=
		Width (FWHM)/eV	1.50	1.50	2.08	1.40	1.91	1.38	=
			(Si2p1/2)/(Si2p3/2)= 0.50						
E4	Etching 2.4 nm	Position/eV	99.7	100.3	101.8	102.9	104.0	707.3	709.1
		Area	4820	2410	4450	261	679	7260	1200
		Width (FWHM)/eV	1.42	1.42	2.29	0.82	1.47	1.43	2.55
			(Si2p1/2)/(Si2p3/2)= 0.50						
E5	Etching 3.0 nm	Position/eV	99.8	100.4	101.8	=	104.0	707.3	709.1
		Area	5320	2680	4370	=	144	10500	2470
		Width (FWHM)/eV	1.35	1.47	3.00	=	2.33	1.43	3.48
			(Si2p1/2)/(Si2p3/2)= 0.50						
E6	Etching 4.2 nm	Position/eV	99.6	100.2	101.8	=	=	707.2	708.9
		Area	6030	3010	3170	=	=	13800	1710
		Width (FWHM)/eV	1.42	1.62	2.89	=	=	1.45	1.65
			(Si2p1/2)/(Si2p3/2)= 0.50						
E7	Etching 5.4 nm	Position/eV	99.7	100.3	101.8	=	=	707.2	709.0
		Area	6240	3120	2710	=	=	16900	5070
		Width (FWHM)/eV	1.33	1.33	2.39	=	=	1.45	2.90
			(Si2p1/2)/(Si2p3/2)= 0.50						
E8	Etching 6.6 nm	Position/eV	99.7	100.3	101.8	=	=	707.2	709.0
		Area	6280	3140	2370	=	=	16900	7800
		Width (FWHM)/eV	1.37	1.41	2.45	=	=	1.48	3.53
			(Si2p1/2)/(Si2p3/2)= 0.50						
E9	Etching 7.8 nm	Position/eV	99.7	100.3	101.8	=	=	707.2	709.0
		Area	6550	3270	2370	=	=	18200	9060
		Width (FWHM)/eV	1.43	1.58	2.62	=	=	12481.80	4.45
			(Si2p1/2)/(Si2p3/2)= 0.50						
Film 2 As	As-depo	Position/eV	99.8	100.4	101.9	=	104.1	707.4	=
		Area	2940	1500	2160	=	4360	2540	=
		Width (FWHM)/eV	0.92	1.00	3.52	=	1.76	1.03	=
			(Si2p1/2)/(Si2p3/2)= 0.51						
E1	Etching 0.6 nm	Position/eV	99.7	100.3	101.8	=	104.0	707.5	=
		Area	2990	1500	4090	=	3550	3200	=
		Width (FWHM)/eV	1.00	0.98	3.39	=	2.16	1.11	=
			(Si2p1/2)/(Si2p3/2)= 0.50						
E2	Etching 1.2 nm	Position/eV	99.7	100.3	101.8	=	104.0	707.3	=
		Area	3540	1770	4710	=	2500	4200	=
		Width (FWHM)/eV	1.04	1.04	3.29	=	2.28	1.16	=
			(Si2p1/2)/(Si2p3/2)= 0.50						
E3	Etching 1.8 nm	Position/eV	99.7	100.3	101.8	=	104.1	707.4	=
		Area	4030	2040	4470	=	1900	7020	=
		Width (FWHM)/eV	1.11	1.16	3.23	=	2.63	1.13	=
			(Si2p1/2)/(Si2p3/2)= 0.51						
E4	Etching 2.4 nm	Position/eV	99.8	100.3	101.8	=	104.1	707.4	709.1
		Area	4680	2330	4080	−	746	7410	3000
		Width (FWHM)/eV	1.13	1.57	3.33	−	2.00	1.17	2.83
			(Si2p1/2)/(Si2p3/2)= 0.50						
E5	Etching 3.0 nm	Position/eV	99.7	100.3	101.8	=	104.1	707.4	709.1
		Area	4930	2480	4350	−	447	9350	1060
		Width (FWHM)/eV	1.10	1.15	3.16	−	2.33	1.16	1.67
			(Si2p1/2)/(Si2p3/2)= 0.50						
E6	Etching 4.2 nm	Position/eV	99.6	100.2	101.7	=	=	707.2	709.0
		Area	5710	2850	2980	=	=	12400	1130
		Width (FWHM)/eV	1.17	1.30	2.96	=	=	1.17	1.33
			(Si2p1/2)/(Si2p3/2)= 0.50						
E7	Etching 5.4 nm	Position/eV	99.7	100.3	101.8	=	=	707.2	709.0
		Area	5990	2990	2130	=	=	13300	2770
		Width (FWHM)/eV	1.20	1.50	2.90	=	=	1.19	2.16
			(Si2p1/2)/(Si2p3/2)= 0.50						
E8	Etching 6.6 nm	Position/eV	99.6	100.2	101.7	=	=	707.2	708.9
		Area	5300	2640	1950	=	=	13600	2340
		Width (FWHM)/eV	1.21	1.56	3.16	=	=	1.08	2.00
			(Si2p1/2)/(Si2p3/2)= 0.50						
E9	Etching 7.8 nm	Position/eV	99.6	100.2	101.7	=	=	707.2	708.9
		Area	5210	2620	2000	=	=	15600	2550
		Width (FWHM)/eV	1.22	1.62	3.16	=	=	1.28	2.00
			(Si2p1/2)/(Si2p3/2)= 0.50						

Film 1

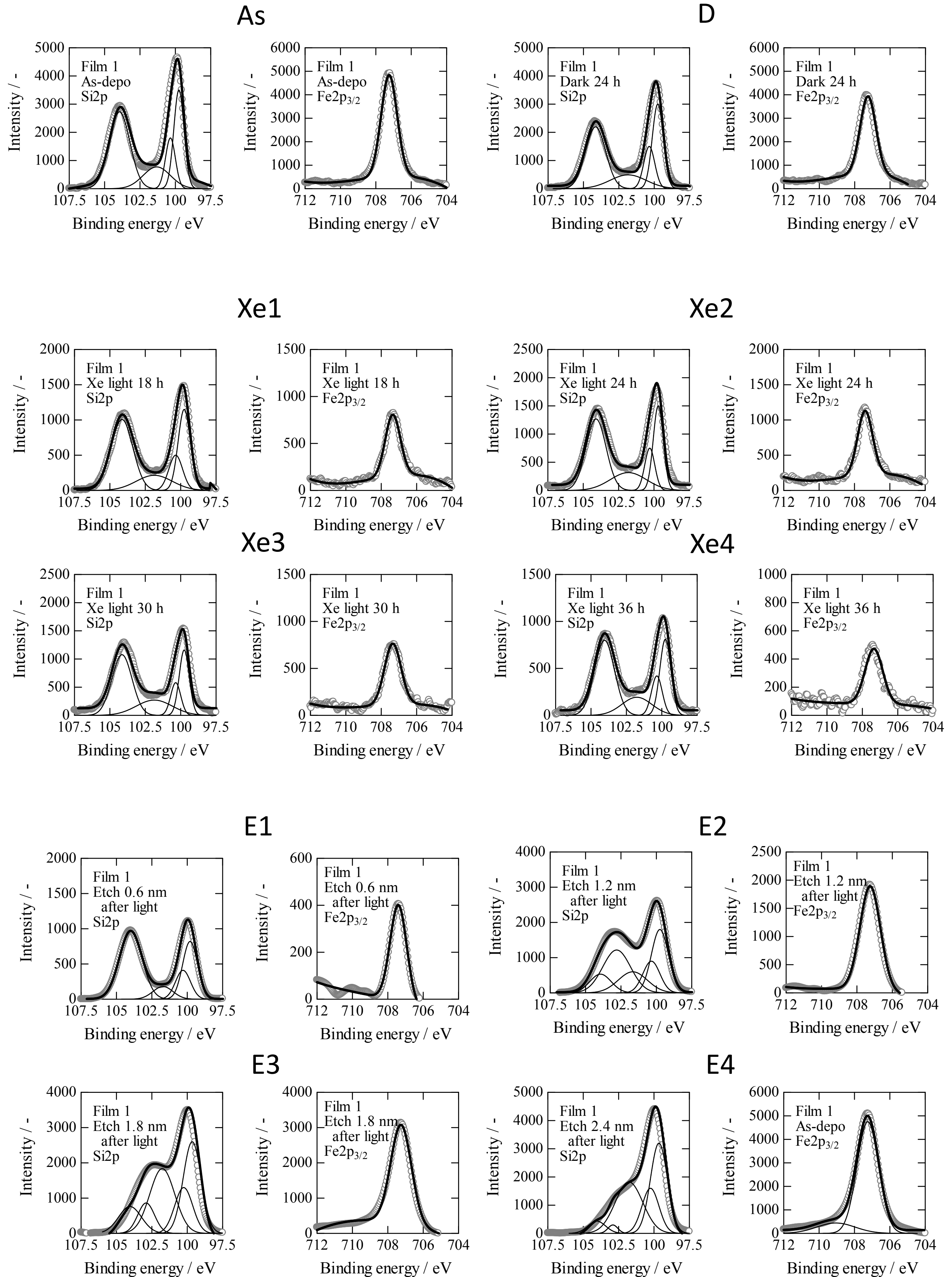

Film 1

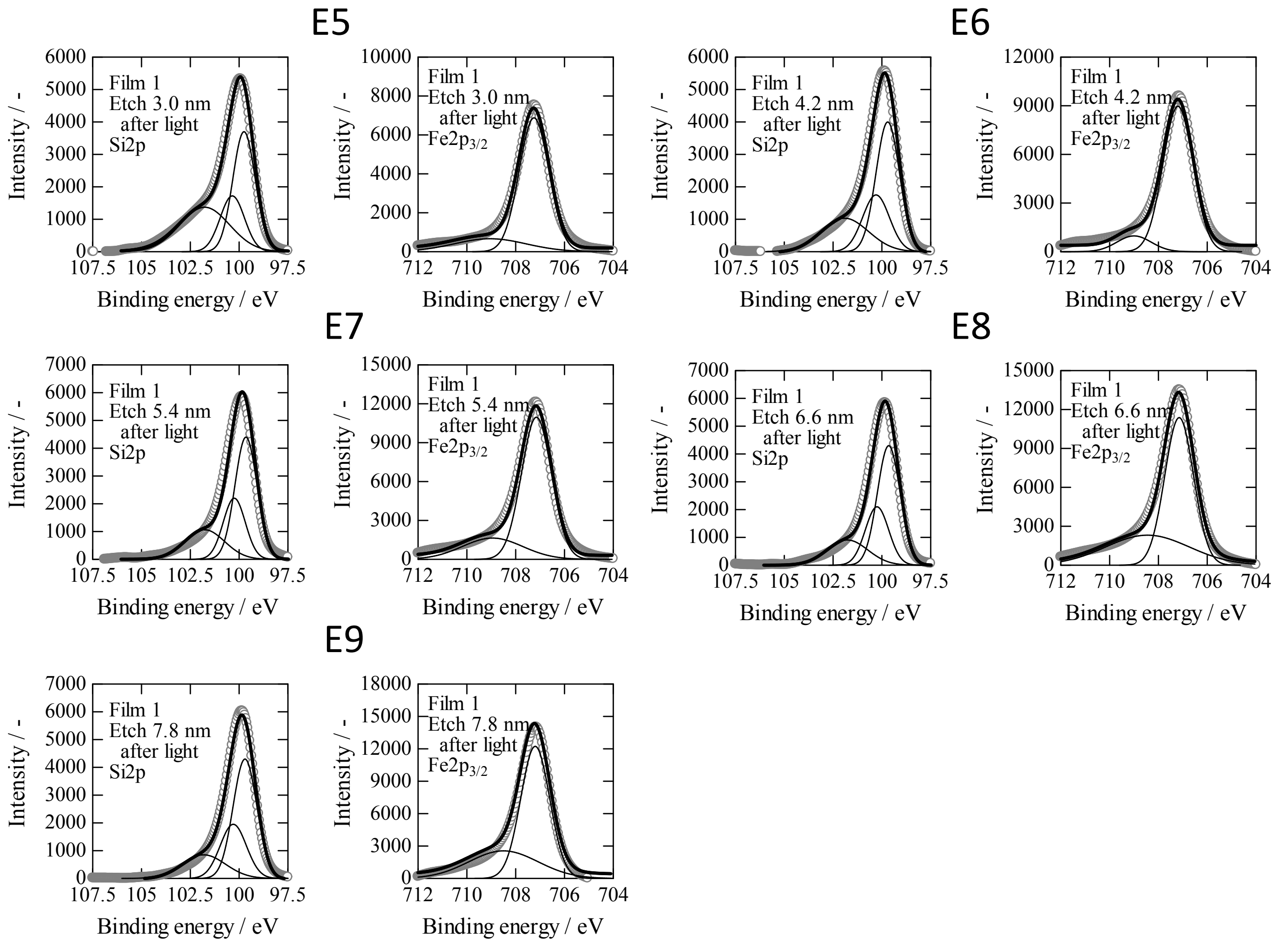

Film 2

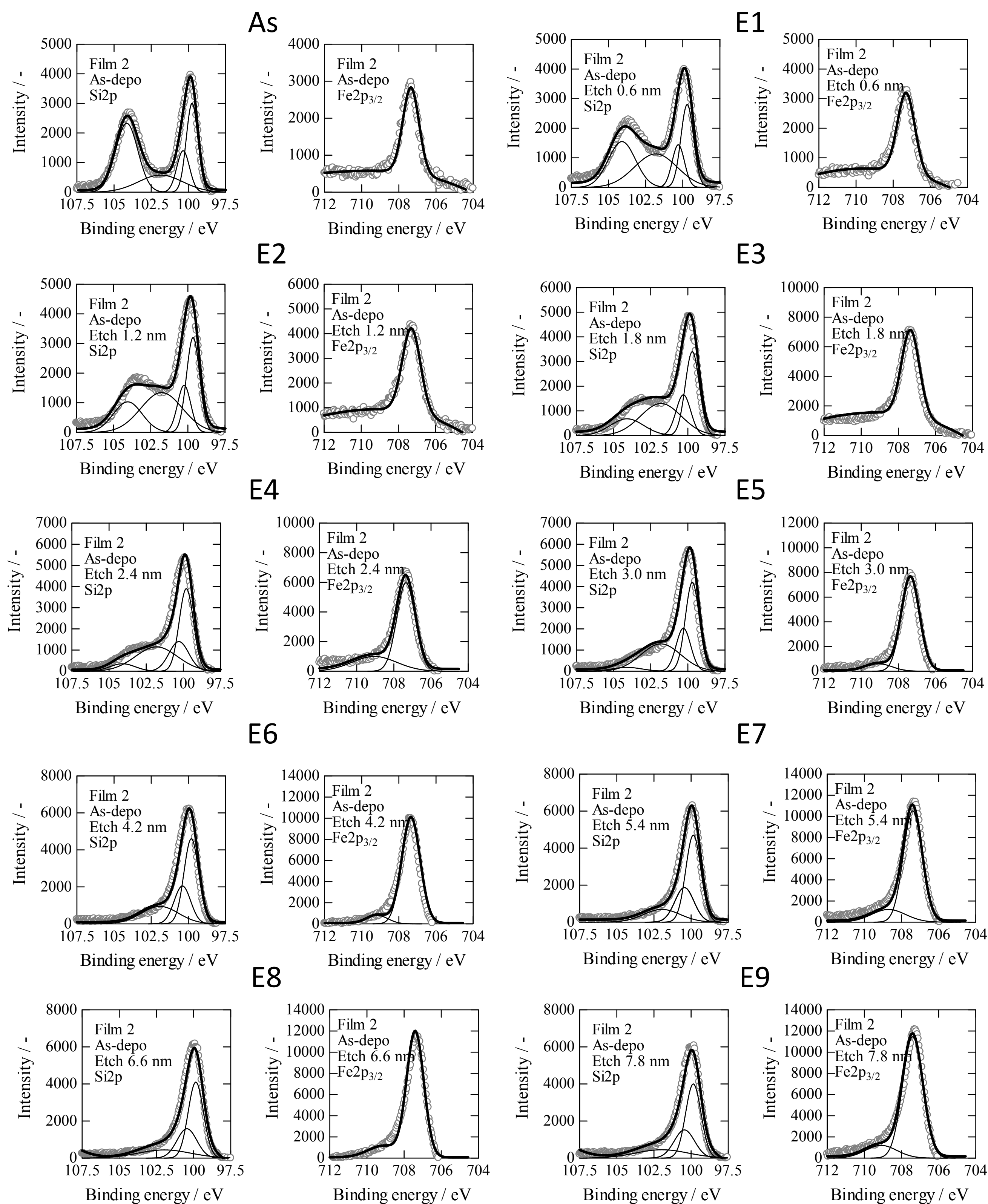

Figure S10. Experimental XPS spectra (open gray circles), fitted curves (black bold lines), and component peaks (thin solid lines) determined by deconvolution of the experimental data for Si 2p (Si $2p_{3/2}$ and Si $2p_{1/2}$) and Fe $2p_{3/2}$.

ESI-7) TEM observations of β-$FeSi_2$ powders before and after photocatalytic reaction (Fig. S11).

A transmission electron microscope (TEM; Tecnai Osiris, FEI Co.) was used for observations of β-$FeSi_2$ particles before and after water-splitting reaction. The TEM images are shown in Fig. S11a (as-pulverized), Figs. S11b and S11c (after reaction), and electron diffraction patterns in Fig. S11d (as-pulverized), Figs. S11e and S11f (after reaction). After water-splitting reaction, something like "beard" was observed on the particle surface. This would be Si-oxide species, detected by XPS as O-Si-O on the surface of the β-$FeSi_2$ thin film. Note that the amount and the thickness of the beard are smaller in Fig. S11b than S11c, which reflects the crystallinity of the particles as shown in Figs. S11e and S11f. The brighter and more symmetrical diffraction pattern in Fig. S11e than S11f indicates more a single crystal-like particle in Fig. S11b than in Fig. S11c. For the XPS measurements, we utilized the β-$FeSi_2$ thin film composed of high quality crystals, similar to the single crystal,[10] thus it was probable that the oxidized layer of the thin film did not exceed ~ 2 nm, indicating that the β-$FeSi_2$ thin film became chemically stable by forming Si-oxide species.

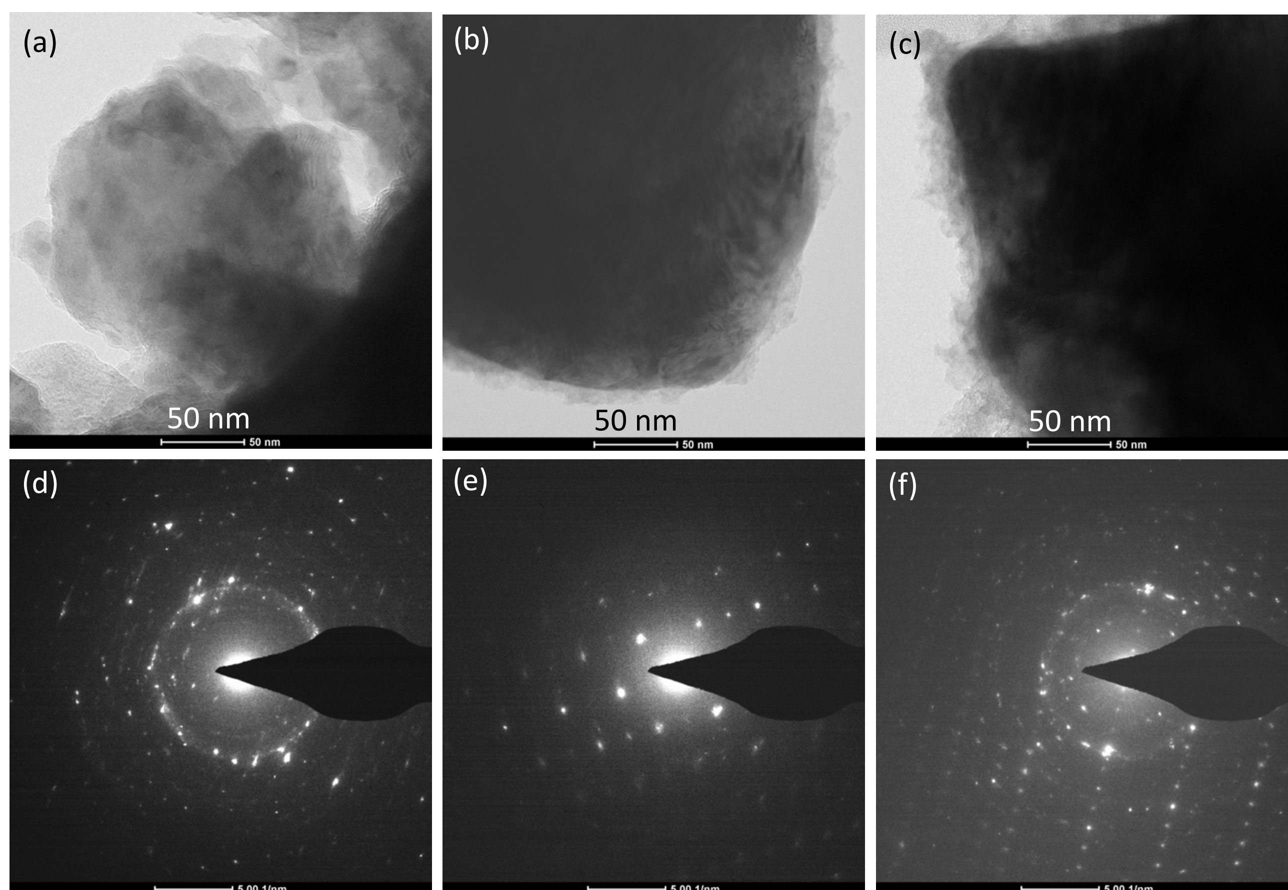

Figure S11. TEM images of as-pulverized β-$FeSi_2$ particles (a), and the particles after water-splitting reaction (b) and (c). Electron diffraction patterns, as-pulverized (d), and after water-splitting reaction (e) and (f).